Model to predict water droplet trajectories in the flow past an airfoil

CrossMark

S. Sor [a], A. García-Magariño [b], A. Velazquez [c],*

[a] *National Institute of Aerospace Technology (INTA), 28850 Madrid, Spain*
[b] *ISDEFE Engineering Systems for Spanish Defense Beatriz de Bobadilla 3, 28040 Madrid, Spain*
[c] *Aerospace Propulsion and Fluid Mechanics Department, Universidad Politecnica de Madrid, Plaza del Cardenal Cisneros 3, 28040 Madrid, Spain*

ARTICLE INFO

ABSTRACT

A theoretical model is presented to predict water droplet trajectories in the flow past an airfoil. The model considers droplet deformation and includes a drag coefficient that accounts for the influence of flow acceleration. This is because, as seen from the reference frame of the droplet, the flow accelerates as the airfoil approaches, even if the airfoil moves at constant velocity. To validate the theoretical model, a series of experimental tests have been carried out in a rotating arm facility. Three parameters were changed in the experiments: 1) the size of the model airfoil (radius of curvature 0.103 m, 0.070 m, and 0.030 m), 2) its velocity (50 m/s, 60 m/s, 70 m/s, 80 m/s, and 90 m/s), and 3) the droplets' initial diameters (in the range from 550 μm to 1050 μm). Comparison between the results obtained using the theoretical model and those collected in the experimental tests (droplet tracking was carried out using a high speed imaging system) showed a good agreement. This suggests that, within the range of parameters that has been tested, the proposed theoretical model could be confidently used for trajectory prediction purposes.

1. Introduction

The problem of predicting liquid droplet trajectories, inside a gas flow is of interest in many fields of science and engineering. They include, among many others, forensic applications [1], solvent extraction [2], electrostatic enhancement of liquid–liquid contacting processes [3], ink-jet printer design [4], spray modeling [5,6], and design of nuclear fusion subsystems [7].

In aeronautics, computation of water droplet trajectories is of interest, among others, for the purpose of simulating icing conditions. As compared to situations in other technical fields, droplet trajectories in these aeronautics-type conditions are characterized by the fact that, in the vicinity of an incoming airfoil, the flow, as seen from the reference frame of the droplet, accelerates with a non-constant acceleration. This is in contrast to other cases in which the flow is either steady or it accelerates with constant acceleration. In this context of dealing with non-constant velocity flows, the interested reader is directed to the work of Rendall and Allen [8] that developed a finite volume code in which droplet motion is tracked using mesh connectivity. This work is of interest because, instead of using a pure Lagrangian approximation, the authors couple the droplet motion to the finite volume computation

of the surrounding flow in a computationally efficient way. Also of interest is the work by Saeed et al. [9] in which the air model of the code is of the panel method type, thereby allowing for a much faster computation of droplet trajectories, albeit at the expense of a smaller accuracy. On the other hand, a comprehensive work that involves both theoretical modeling and experimental testing has been reported by Papadakis et al. [10]. Additional experimental data in the field can be accessed in the study published by Reehorst and Ibrahim [11].

With regard to the basic Fluid Mechanics aspects of the modeling of droplet trajectories, it is worth mentioning, first, the review article by Aggarwal and Peng [12] published in 1995. In Section 1 of that article, the authors review a number of droplet dynamic models and conclude that flow non-uniformity and acceleration affect the aerodynamics forces critically. Also, they report a large uncertainty regarding their actual contribution to the total drag and lift forces. Even though it is not a review article by itself, reference [13] by Schmehl also contains a quite interesting discussion on droplet drag and dynamics models, including those models that deal with flow non-uniformity and acceleration. A method to reduce the number of similarity parameters needed to close a droplet trajectory model (under certain assumptions) has been published by Bragg [14]. In the case of unsteady Stokes flow, Maxey and Riley [15] have proposed a generalized equation of motion for a sphere in a non-uniform flow. In the case of an inviscid unsteady non-uniform flow, Auton et al. [16] have derived

---

* Corresponding author.
E-mail address: angel.velazquez@upm.es (A. Velazquez).

a general expression for the fluid force on the body. The case of drop deformation under steady conditions for a variety of fluids other than water has been extensively studied experimentally by Hsiang and Faeth [17]. Empirical correlations for the drag coefficient of gas bubbles inside a liquid (the opposite case to the one presented here) have been reported by Zhang et al. [18]. A statistical approach to droplet trajectory prediction during aerodynamics fragmentation has been developed by Flock et al. [19]. Regarding the fundamental aspects of droplet deformation that, in turn, affect droplet trajectory, the reader is directed to the excellent review presented by Theofanous [20]. In this review article, apart from making a critical review of the literature, the author proposes the existence of two fundamental droplet deformation modes that may explain the large variety of available experimental observations with regard to the shapes of the deformed droplets. From the standpoint of novel experimental techniques it is worth mentioning the work of Zarrabeitia et al. [21] that have recently developed a stereo reconstruction technique that allows for the recording of 3D droplet trajectories. Also, it is also important to refer to the work of Theofanous and Li [22] in which the authors present their laser-induced fluorescence technique.

Finally, and because of their relevance for the present work, it is important to discuss in some detail the studies presented by Temkin and Metha [23], Igra and Takayama [24], and Jourdan et al. [25]. The article by Temkin and Metha [23] presents an experimental study on the motion of water droplets inside accelerating and decelerating flows. The interesting modeling aspect of this study is that the authors assume a functional relationship between the drag coefficient and the so called acceleration parameter that is defined as the time derivative of the slip velocity divided by the square of the slip velocity itself. The experiments were carried out in a shock tube. Droplet diameters were in the range from 100 μm to 200 μm, which led to Weber numbers such that the authors assumed a negligible droplet deformation. Their conclusion (which is in contradiction with some other studies published in the literature) is that the unsteady drag of a sphere in decelerating flow is always larger than the steady drag at the same Reynolds number, while is it always smaller if the surrounding flow accelerates. Igra and Takayama [24] also used a shock tube facility but, in their case, with non-deformable spheres made up of polystyrene, nylon, and polyamide. Their diameter ranged from 0.5 mm to 4.8 mm. The Reynolds number covered in their experiments was in the range down from 6000 up to 100,000. Incident Mach numbers in the shock tube were 1.27, 1.50, and 1.80. In their conclusions, the authors reported unsteady drag values about 50% larger than the corresponding steady values in these shock tube conditions. More recently, Jourdan et al. [25] have presented another quite comprehensive experimental study based, also, on a shock tube type test rig. They used non-deformable spheres (made of either polystyrene or nylon) with diameters ranging from 500 μm to 6.6 mm. In their tests, the authors found that the unsteady drag is always larger than the steady drag at the same Reynolds number and explicitly stated at the end of their "Results and Discussion" section (section 4) that the acceleration parameter proposed by Temkin and Metha [23] may not be the relevant characteristic parameter for the flows that they considered. Even though these two experimental studies presented some differences that might affect the conclusions (droplet were deformable in reference [23] and non-deformable in reference [24], and velocities, and associated compressibility effects, were also somewhat different) the conclusion is that the field still is quite alive and that no definite conclusions are available so far.

The novelty of the work presented in this article consists of proposing a new theoretical model on droplet deformation and trajectory that is validated afterwards in a series of experimental tests in a rotating arm facility. The model, formulated as a set of
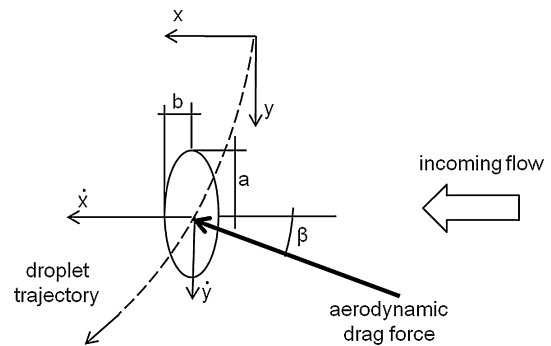

Fig. 1. Sketch of the problem under consideration.

three ordinary differential equations involves the presence of the so-called acceleration parameter (already proposed, and contested, also, by other researchers) and an equation for the deformation of the droplet. Then, the specific novelty aspects of the study are twofold: a) both the acceleration parameter and the droplet deformation equation enter simultaneously into the model (previous studies considered non-deformable droplets only), and b) because of this, although the functional form of the acceleration parameter is hypothesized, its actual parametric dependency needs to be characterized, and this is done via experimental testing.

Regarding the organization of the present article the theoretical model is presented in Section 2. The experimental rotating arm rig is described in Section 3. Model and experimental results are compared and discussed in Section 4 and, finally, conclusions are presented in Section 5.

2. Theoretical model

It is assumed that the droplet motion is governed by three equations: two dynamics equations (1)–(2) that represent the equilibrium of forces in the horizontal (x) and vertical (y) directions, and one equation (3) that models the droplet deformation. This equation (3) influences the droplet drag force because, indirectly, it allows for the computation of the droplet cross-section area normal to the incoming flow. Fig. 1 shows a sketch of both the acting forces and the axis of coordinates. The coordinates' axes (fixed in space) are located in the droplet centre of mass at the precise moment when it enters the measurement window.

Apart from some other considerations, the model presented hereafter is based on three main hypotheses that have been verified analyzing the experimental data obtained during the completion of the experimental campaigns. These hypotheses are:

- The "y" component of the incoming airflow $|V_{air\_y}|$ is very small ($V_{air\_y} \cong 0$). This assumption (that also implies that $|V_{air\_x}| \gg |V_{air\_y}|$) means that the model is valid, only, in the vicinity of the stagnation streamline (stagnation region) of the incoming airfoil.
- It is assumed that the droplet deforms as an oblate spheroid.
- Because of the first hypothesis, the slip velocity in the horizontal direction is much larger than the slip velocity in the vertical direction (this is, of course, not true during the initial instants of the droplet trajectory but velocities are very low and droplet deformation is negligible at these stages). Then, it is further hypothesized that the droplet deforms, only, along the vertical direction that is perpendicular to the direction of the much larger horizontal slip velocity. The practical implication of this third hypothesis is that forcing terms in the equation that models droplet deformation (equation (3)) depend, only, on the horizontal slip velocity; thereby decoupling, effectively, the "x" equation of motion (equation (1)) and the

equation for droplet deformation (equation (3)) from the "y" equation of motion (equation (2)).

Now, the three model equations are:

$$m_d \frac{d^2 x}{dt^2} = F_{drag\_x} \tag{1}$$

$$m_d \frac{d^2 y}{dt^2} = -F_{drag\_y} + m_d g \tag{2}$$

$$\frac{3\,m_d}{16} \frac{d^2 a}{dt^2} = +F_v + F_{st} + F_P \tag{3}$$

where:

- x, y, a, and t are the coordinates of the droplet centre of mass, the half-maximum dimension of the deformed droplet, and time respectively.
- m_d is the droplet mass equal to $4\pi \rho R_d^3/3$ (R_d is the initial droplet radius), g is the gravity acceleration and ρ_d is the water density.
- F_{drag_x}, F_{drag_y}, F_v, F_{st}, and F_P are the "x" and "y" components of the aerodynamics drag force, the viscous force and surface tension force that oppose droplet deformation, and the flow pressure force that acts on the droplet surface respectively.

The aerodynamic drag forces F_{drag_x} and F_{drag_y} depend on the slip velocities V_{sx} and V_{sy} defined as:

$$V_{sx} = V_{air\_x} - \frac{dx}{dt}, \qquad V_{sy} = \frac{dy}{dt} \tag{4}$$

It has been assumed previously that $V_{sx} \gg V_{sy}$. Then, if β is the angle between the total drag force and the "x" axis, the following approximations hold: $\sin\beta \cong V_{sy}/V_{sx}$ and $\cos\beta \cong 1$. Then, F_{drag_x} in equation (1) can be modeled as:

$$F_{drag\_x} \cong \frac{1}{2}\rho_{air} V_{sx}^2 \pi a^2 C_D \tag{5}$$

where ρ_{air} is the air density and C_D is the drag coefficient. Now, the modeling of this drag coefficient is the most critical aspect of the formulation presented in this section. Specifically, it was decided that $C_D = C_{D1} + C_{D2}$, where C_{D1} and C_{D2} model steady and unsteady effects respectively as follows:

$$C_{D1} = C_{D_{sphere}}^{b/a} \cdot C_{D_{disk}}^{1-b/a} \tag{6}$$

$$C_{D2} = k \frac{b}{V_{sx}^2} \frac{dV_{sx}}{dt} \tag{7}$$

where $C_{D_{sphere}}$ is the known drag coefficient of a perfect sphere based on a Reynolds number defined using the instantaneous (time dependent) slip velocity as the characteristic velocity, and the instantaneous (time dependent) droplet maximum elongation: "2a" (see Fig. 1), as the characteristic length. $C_{D_{disk}}$ is the drag coefficient of a disk whose value, assumed to be constant in the range of Reynolds numbers considered, is taken to be 1.17. In practice, relation (6) assumes that the quasi-steady part of the droplet drag coefficient is obtained by interpolating between the drag of a perfect sphere and the drag of a disk. The parameter that controls the interpolation is the droplet aspect ratio b/a, see Fig. 1. Since the droplet has constant known volume, V_d, the values of "a" (obtained from equation (3)) and "b" are related by a simple geometry relation: $V_d = (4\pi/3)a^2 b$ that means $R_d^3 = a^2 b$. Relation (7) assumes that the unsteady part of the droplet drag coefficient depends on the functional $(1/V_{sx}^2)dV_{sx}/dt$ that is directly related to the acceleration parameter as defined by Temkin and Metha

[23]. The main difference here with the formulation of Temkin and Metha [23] is that, in the present model, C_{D2} depends, also, on the instantaneous (time dependent) droplet elongation "b" in the "x" direction. k is a calibration coefficient that in the range of experimental cases that have been tested (that will be described in the next section) has been found to be constant and equal to 9. Possibly, the most critical aspect of the model being presented has to do with relations (6) and (7). These two relations describe separately the steady and unsteady parts of the problem, but it might be natural to think that a more general single formulation (not divided into two different terms) should exist. However this generalization is out of the scope of the present article. The second question is that in the formulation of the steady part, the dimensionless parameter that controls the drag coefficient is the droplet deformation ratio b/a. It was found that this formulation yields a model that agrees fairly well with the experimental data but, obviously, it was not possible to provide a plausible physical explanation for this specific selection at this stage. It could have been, for example, the same ratio elevated to some power.

Within the same set of hypotheses, F_{drag_y} in equation (2) can be approximated as:

$$F_{drag\_y} \cong \frac{1}{2}\rho_{air} V_{sx} V_{sy} \pi a^2 C_D \tag{8}$$

Finally, the three terms in the right hand side of equation (3) are modeled as follows:

$$F_v = -\frac{64}{9}\mu_d \pi R_d^3 \frac{1}{a^2} \frac{da}{dt} \tag{9}$$

where μ_d is the droplet viscosity. This term, as described by Sor and Garcia-Magariño [26], represents the force that viscosity opposes to droplet deformation. It has been included into equation (3) for the sake of completion. However, for the range of parameters considered in the experimental tests, its actual value was found to be much smaller than the other two terms in the right hand side of equation (3). If a different fluid is chosen for the tests, for instance: glycol that has much higher viscosity than water, this term becomes comparable to the other two terms. Then, since this model will deal with water droplets only, this viscous term will be dropped altogether from the formulation:

$$F_{st} = -\frac{4}{3}\sigma \frac{dA_d}{da} \tag{10}$$

This term, as described by Sor and Garcia-Magariño [26], represents the force that surface tension opposes to droplet deformation. σ is the water surface tension and A_d is the surface area of the droplet. dA_d/da represents the rate of variation of droplet surface area with respect to the maximum elongation for a constant volume droplet. Since the deformed droplet is assumed to have the shape of an oblate spheroid, the derivative dA_d/da can be obtained by purely geometrical considerations. In particular:

$$\frac{dA_d}{da} = 4\pi a - \frac{4\pi R_d}{\varepsilon (a/R_d)^5} \ln\left(\frac{1+\varepsilon}{1-\varepsilon}\right)$$
$$+ \frac{3\pi R_d}{\varepsilon (a/R_d)^{11}} \left[\frac{2}{\varepsilon(1-\varepsilon^2)} - \frac{1}{\varepsilon}\ln\left(\frac{1+\varepsilon}{1-\varepsilon}\right)\right] \tag{11}$$

where $\epsilon = [1 - (b/a)^2]^{1/2}$. Note that dA_d/da is a known functional that depends on the variable a only. For the reminder of the article this functional will be referred to as (a).

The last term in equation (3) represents the pressure force that the incoming flow exerts on the droplet, Sor and Garcia-Magariño [26]. The actual effect of this term is to promote deformation:

$$F_P = \frac{1}{2}C_P \rho_{air} V_{sx}^2 \pi R_d^2 \tag{12}$$

where C_P is a pressure coefficient that has been calibrated and that has a constant value of 0.93. This pressure term should be the integral of a local pressure times a differential surface area and, therefore, it cannot be computed as such since the droplet surface local pressure distribution is unknown. This is the reason why relation (12) represents a global approximation to that integral. It could be argued that F_P in relation (12) should scale with a^2 instead of R_d^2 ($a > R_d$). However, as discussed by Ibrahim et al. [27], the fact that pressure decreases sharply up from the droplet stagnation streamline region down to the droplet edge region suggests that scaling with a parameter smaller than a might be more appropriate. Note that within the hypothesis of this model, relation (12) involves V_{sx} only and not V_{sy} that means, as mentioned earlier, that equations (1) and (3) are effectively decoupled from equation (2). The initial conditions for equations (1)–(3) are:

$$x(0) = 0, \quad \left(\frac{dx}{dt}\right)_{t=0} = 0 \tag{13}$$

$$y(0) = 0, \quad \left(\frac{dy}{dt}\right)_{t=0} = V_0 \tag{14}$$

$$a(0) = R_d, \quad \left(\frac{da}{dt}\right)_{t=0} = 0 \tag{15}$$

where V_0 is the droplet falling velocity when it enters the test window. In an actual generic case, it should be taken equal to the terminal falling velocity of the droplet.

Now, it is convenient to re-write equations (1)–(3) in dimensionless form. To this end, the following dimensionless variables and parameters are defined:

$$\eta = \frac{x}{R_d}, \quad \zeta = \frac{y}{R_d}, \quad \alpha = \frac{a}{R_d}, \quad \tau = \frac{t U_m}{R_c} \tag{16}$$

$$\mathbb{V}_{sx} = \frac{V_{sx}}{U_m}, \quad \mathbb{V}_{sy} = \frac{V_{sy}}{U_m}, \quad \mathbb{A}_d = \frac{A_d}{R_d^2}, \quad \mathbb{F}(\alpha) = \frac{F(a)}{R_d} \tag{17}$$

where U_m is the airfoil velocity and R_c its radius of curvature. Using this new change of coordinates, the model equations and initial conditions are written as:

$$\frac{d^2\eta}{d\tau^2} = \Pi_1 \mathbb{V}_{sx}^2 \alpha^2 \left[\left(C_{D_{sphere}}^{(R_d/a)^3} \cdot C_{D_{disk}}^{1-(R_d/a)^3} \right) + \left(\Pi_2 \frac{1}{\alpha^2 \mathbb{V}_{sx}^2} \frac{d\mathbb{V}_{sx}}{d\tau} \right) \right] \tag{18}$$

$$\frac{d^2\zeta}{d\tau^2} = -\Pi_1 \alpha^2 \mathbb{V}_{sx} \mathbb{V}_{sy} \left(C_{D_{sphere}}^{(R_d/a)^3} \cdot C_{D_{disk}}^{1-(R_d/a)^3} \right) + \Pi_3 \tag{19}$$

$$\frac{d^2\alpha}{d\tau^2} = -\Pi_4 \mathbb{F}(\alpha) + \frac{16}{3} \Pi_1 C_P \mathbb{V}_{sx}^2 \tag{20}$$

where:

$$\Pi_1 = \left[\frac{3}{8} \frac{\rho_{air}}{\rho_d} \left(\frac{R_c}{R_d} \right)^2 \right] \tag{21}$$

$$\Pi_2 = \frac{k R_d}{R_c} \tag{22}$$

$$\Pi_3 = \frac{g R_c}{U_m^2} \left(\frac{R_c}{R_d} \right) \tag{23}$$

$$\Pi_4 = \frac{16}{3\pi} \frac{\sigma}{\rho_d} \left(\frac{R_c}{U_m R_d} \right)^2 \frac{1}{R_d} \tag{24}$$

The dimensionless initial conditions are:

$$\eta(0) = 0, \quad \left(\frac{d\eta}{d\tau}\right)_{\tau=0} = 0 \tag{25}$$

$$\zeta(0) = 0, \quad \left(\frac{d\zeta}{d\tau}\right)_{\tau=0} = \frac{R_c}{R_d} \frac{V_0}{U_m} \tag{26}$$
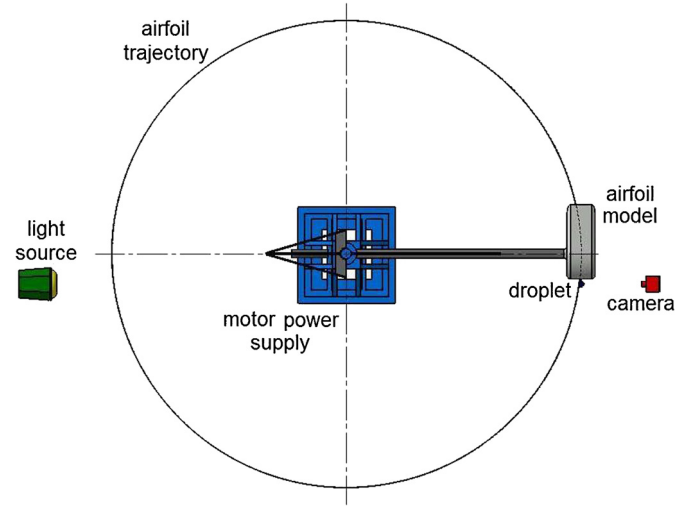

Fig. 2. Top view (sketch) of the rotating arm facility.

$$\alpha(0) = 1, \quad \left(\frac{d\alpha}{d\tau}\right)_{\tau=0} = 0 \tag{27}$$

Numerical integration of equations (18) and (20) with initial conditions (25) and (27) is straightforward. Then, after $x(t)$ and $a(t)$ have been obtained $b(t)$ is easily computed and equation (19) together with initial condition (26) can be integrated. In the experimental test cases described in the next section, V_0 in initial condition (26) was close to the terminal falling velocity of the droplets. This means that the droplet vertical velocity in the test window was nearly constant. In fact, the tracking equipment was not able to detect significant changes in this vertical velocity.

3. Description of the experimental setup

The experimental campaign to examine the droplet trajectory model has been carried out at the INTA rotating arm facility in Spain. A detailed description of this facility has been published by the authors in a previous article [28]. In any case, and for the sake of completion, a shortened account of its characteristics is presented in this section.

The facility, see Figs. 2 and 3, consists of an electric motor, a support structure and a rotating arm that has a length of 2.2 m. The engine axis is vertical which means that airfoils placed at the arm's end describe a circular trajectory with diameter of 4.4 m in a horizontal plane. The whole setup is placed inside a room whose dimensions (length, width and height) are 6.8 m, 6.6 m, and 2.7 m, respectively. At maximum power, the electrical motor can rotate at 400 rpm which means the maximum attainable airfoil velocity is 90 m/s (Mach 0.26).

Three Styrofoam airfoils were used in the experiments. They were labeled M1, M2 and M3 and their geometry parameters are specified in Table 1.

The airfoils were rather blunt to simulate those used for commercial aircraft applications. Their dimensionless coordinates can be found in reference [28]. The droplet generator was a monosized TSI MDG-100. The discharge could be varied between 2.2 cm^2/min and 51.79 cm^2/min. For the present experimental campaign, three different ranges of droplets diameter were selected. They were 575 μm ± 25 μm, 775 μm ± 25 μm and 1025 μm ± 25 μm. These specific ranges were obtained by means of acting on both the jet mass flow rate of the droplet generator and on the frequency of the piezoelectric. The optical camera was a Photron SA-5. Its capturing rate ranged from 10^3 frames per second (fps) to 10^6 fps. In the present campaign, the capturing rate was selected to be 75,000 fps with a resolution of 192×312 pixels. Also, extra lenses

Fig. 3. Actual picture of the rotating arm facility.

Table 1
Geometry parameters of the three airfoils: M1, M2, and M3.

Model	Chord	Leading edge radius	Thickness
M1	0.690 m	0.103 m	0.276 m
M2	0.468 m	0.070 m	0.187 m
M3	0.199 m	0.030 m	0.080 m

were used for additional magnification of the images. Characterization of the flow field was performed by using a Particle Image Velocimetry system (PIV). It was TSI System with illumination provided by two pulsed Nd-Yag 190 mJ lasers. A Power View Plus 4MP camera was used to record the images with a resolution of 2048×2048 pixels. Camera lenses were AF-S VR Micro Nikkor 105 mm f/2.8 G IF-ED Nano Crystal Coat, AF Nikkor 80–200 mm f/2.8 D IF-ED, and Nikkor 50 mm f/1.4. Particles used to sow the flow were olive oil droplets having a diameter of 1 μm. The TSI Insight 3G software was used for synchronized of image capturing, flow illumination, and the subsequent analysis. Sampling of the flow field was carried out at frequencies in the range from 4.75 Hz to 6.5 Hz. Time between two consecutive laser pulses varied between 1.1 μs and 200 μs. At 34 μs (the time used for the fastest moving airfoil) PIV particle moved about 3 mm that is a distance much smaller than the characteristic length of the problem that is the airfoil leading edge radius (103 mm, 70 mm and 30 mm respectively). PIV interrogation areas were divided into smaller sub-interrogation areas for analysis purposes. The spatial flow field resolution in the test windows near the airfoil leading edges was of the order of 1 mm. Additional details on the specifics of the PIV analysis can be found in reference [28].

The summary of the 45 tests cases addressed in the experimental campaign is provided below. The values of the different dimensionless parameters of the theoretical model (Π_1, Π_2, Π_3, and Π_4, see relations (21)–(24)) are also given:

- Three droplet diameters: 575 μm, 775 μm, and 1025 μm
- Three airfoils leading edge radii: 0.103 m, 0.070 m, 0.030 m
- Five airfoil velocities: 50 m/s, 60 m/s, 70 m/s, 80 m/s, and 90 m/s
- Range of Π_1: 0.38 to 14.5
- Range of Π_2: 0.05 to 0.31
- Range of Π_3: 0.001 to 0.072
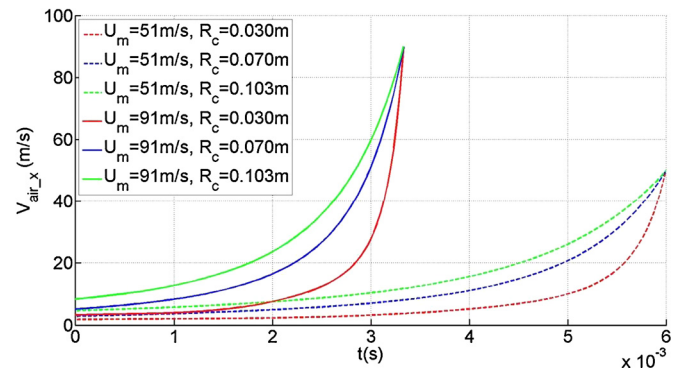- Range of Π_4: 0.012 to 2.770

Fig. 4. Velocity time histories at the stagnation streamline for thee airfoil models (M1, M2 and M3) at translational velocities of 51 m/s and 91 m/s.

The flow field velocity and acceleration time histories were characterized in the absence of falling water droplets. This means that, implicitly, a one way interaction approach was considered [29]. The methodology used to obtain the different velocity field in the airfoil reference frame out of a series of consecutive PIV standing frames is described in reference [28]. 15 different flow velocities and acceleration profiles were used in the experimental campaign. This corresponds to three airfoil models (M1, M2 and M3) and five translational velocities for each of them (see Table 1). In practice, from the droplet trajectory model point of view, this means that 15 different flow velocity and acceleration profiles could be used for testing purposes. To give an impression of the range that was actually covered, the stagnation stream line histories of flow velocity at the extremes of the velocity range (50 m/s to 90 m/s) for the three airfoil models are presented in Fig. 4. The acceleration histories for these cases are presented in Fig. 5.

A large number of samples were taken for each of the 45 test cases. An experimental uncertainty analysis in the flow velocity characterization is summarized in Figs. 6 and 7. Fig. 6 presents the three uncertainty bars associated to the 3 limiting velocity profiles corresponding to 90 m/s of maximum airfoil velocity as presented in Fig. 4. These bars were obtained using all recorded velocity profiles to calculate the standard deviation and plotting this standard deviation band. The typical spread was of the order of ±0.8 m/s that for an average velocity in the range between 20 m/s and 40 m/s (see Fig. 6) yields and uncertainty of the order of ±2% to ±4%. Fig. 7 shows the kernel density estimate of
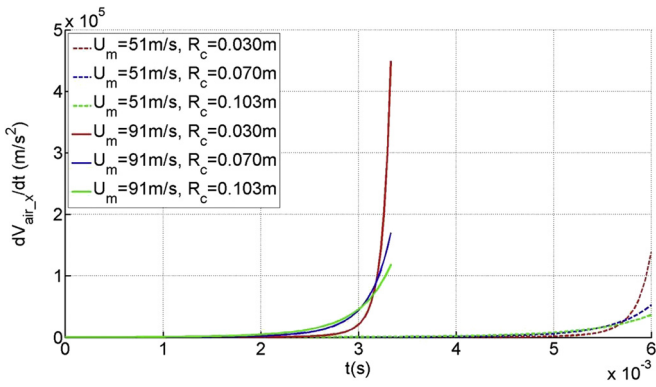
Fig. 5. Acceleration time histories at the stagnation streamline for thee airfoil models (M1, M2 and M3) at translational velocities of 51 m/s and 91 m/s.
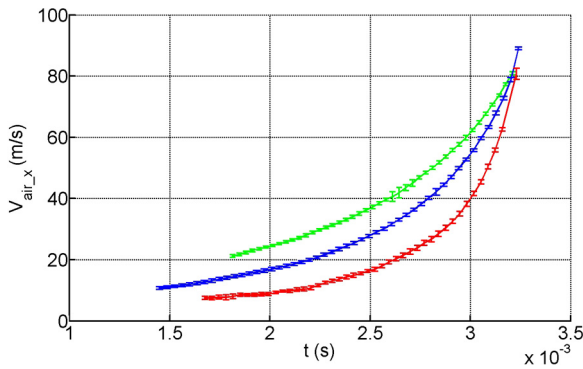

Fig. 6. Uncertainty bars associated to three velocity profiles ($U_m = 91$ m/s) presented in Fig. 4.
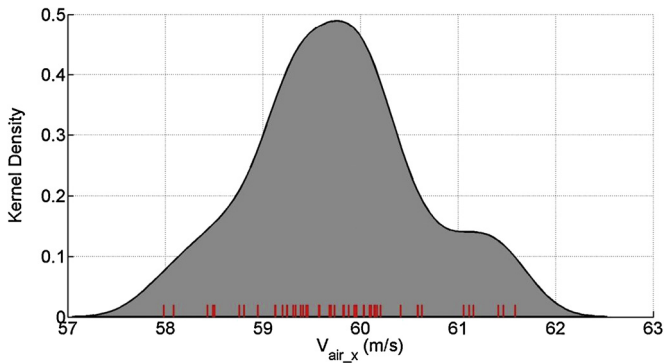

Fig. 7. Kernel density estimate of the measurement at time 3 ms in the case of intermediate airfoil (M2) at the maximum airfoil velocity (91 m/s).

Fig. 8. Results corresponding to three different measurements of the droplet trajectory of the same experimental case: $R_c = 0.070$ m, $R_d = 388$ μm, and $U_m = 71$ m/s.

Fig. 9. Comparison between experimental and theoretical results for the case of $R_c = 0.030$ m, $R_d = 288$ μm, and two airfoil velocities: $U_m = 51$ m/s, and $U_m = 91$ m/s.

Fig. 10. Counterpart of Fig. 8 for $R_c = 0.103$ m, $R_d = 288$ μm, and $U_m = 51$ m/s, and $U_m = 91$ m/s.

the 50 measurement at time 3 ms in the case of intermediate airfoil (M2) at the maximum velocity (90 m/s) calculated by MATLAB. The kernel density estimation is a non-parametric way to estimate the probability density function of a random variable [30]. The rug plot of the measurements is super-imposed on the kernel density estimate plot.

Regarding the uncertainty associated to the measurement of droplet trajectories, Fig. 8 shows a sample of three different measurements of the case with $R_c = 0.070$ m, $R_d = 388$ μm, and $U_m = 71$ m/s. It can be observed that, initially, the droplets moved in the negative "x" direction, see Fig. 1. This is because the droplet generator did not always discharge droplets with a purely vertical velocity. In fact, in some cases, some residual horizontal velocity was present as the droplet left the generator (sometimes along the positive x direction and sometimes along the negative one). In any case, as the airfoil approached the droplet, the slip velocity began
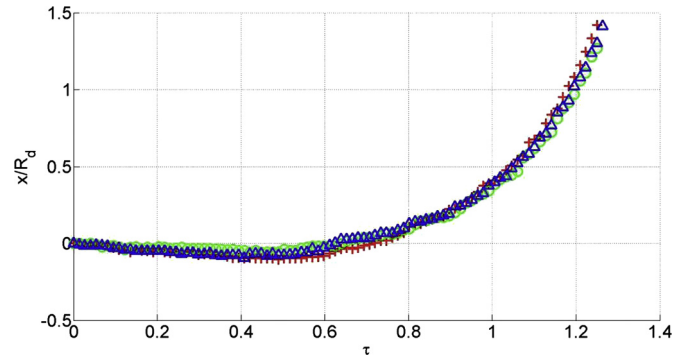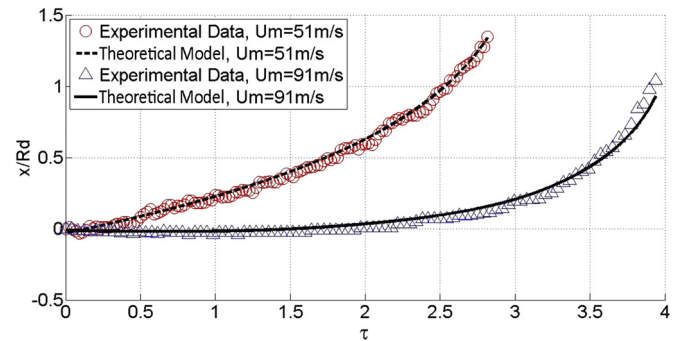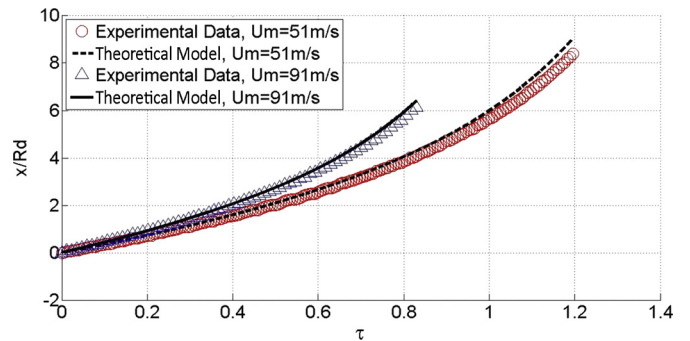
to increase sharply and the droplet moved in the positive "x" direction.

4. Results

Comparison between the experimental results and those obtained by applying and solving numerically the theoretical model has been carried out for all 45 cases described in the previous section. Here the results obtained for the 8 limiting cases that combine the largest and smallest values of droplet diameter, airfoil leading edge radius, and airfoil velocity are presented ($2^3 = 8$ cases) in Figs. 9, 10, 11 and 12. It could be observed that, in general, there is a reasonably good agreement between the measured and computed droplet trajectories. Typically, the larger discrepancies tend to occur at the late time instants of the trajectories and, also, for the smaller droplets. The reason could be that in those instants, both the slip velocity and the flow acceleration achieve their largest values and this decreases the accuracy of the experi-
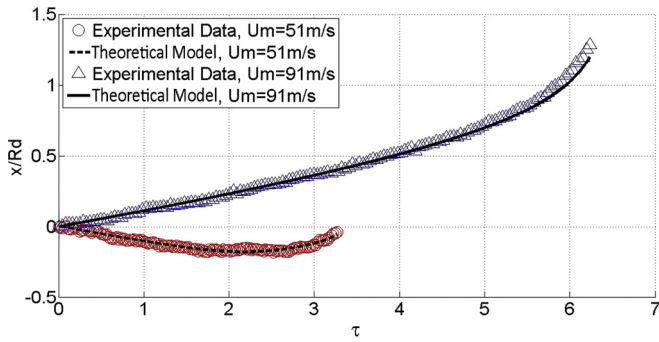
Fig. 11. Counterpart of Fig. 8 for $R_c = 0.030$ m, $R_d = 513$ μm, and $U_m = 51$ m/s, and $U_m = 91$ m/s.
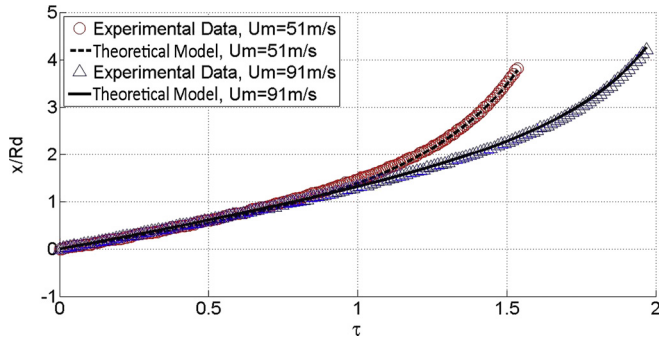

Fig. 12. Counterpart of Fig. 8 for $R_c = 0.103$ m, $R_d = 513$ μm, and $U_m = 51$ m/s, and $U_m = 91$ m/s.

Table 2
Discrepancy between measured and theoretical droplet trajectories for the 8 limiting cases presented in Figs. 9 to 12.

Model	U_m (m/s)	R_d (μm)	Mean (Ω)	Std (Ω)
M1	51	294	3,64	3,99
M1	51	520	1,98	1,14
M3	51	291	2,54	1,76
M3	51	523	2,54	1,69
M1	91	286	2,78	2,68
M1	91	525	1,00	0,88
M3	91	299	2,17	1,85
M3	91	501	2,55	2,83

mental droplet tracking system. At the same time, smaller droplets are more difficult to track because they fill in a smaller number of pixels in the camera.

It is important, nevertheless to quantify the discrepancies between the measured and computed droplet trajectories. This has been done for all 45 experimental tests cases. The criterion was to compute, for each case, a figure of merit Ω defined as the difference (for each time) between the experimental and theoretical "*x*" droplet displacement divided by the maximum experimental value. The results of the most critical cases are presented in Table 2 (the Standard deviation is also included). There, it could be observed that the average discrepancy was of the order of 3.6% at most. The maximum discrepancy Ω for all cases was 15%.

Now, it is shown how the droplet deformations obtained from the theoretical model compare to the experimental data. This has been done selecting some cases and solving the model equations. Then, the theoretical results are compared to the experimental tracking of the droplet trajectories and, also, to the images obtained with camera system. A comparison for two different cases: a) $R_c = 0.103$ m, $R_d = 513$ μm, and $U_m = 91$ m/s, and b) $R_c = 0.070$ m, $R_d = 388$ μm, and $U_m = 71$ m/s is presented in Fig. 13. The comparison has been performed superimposing the computed theoretical shape (drawn using a white line in a pixel-wise basis)
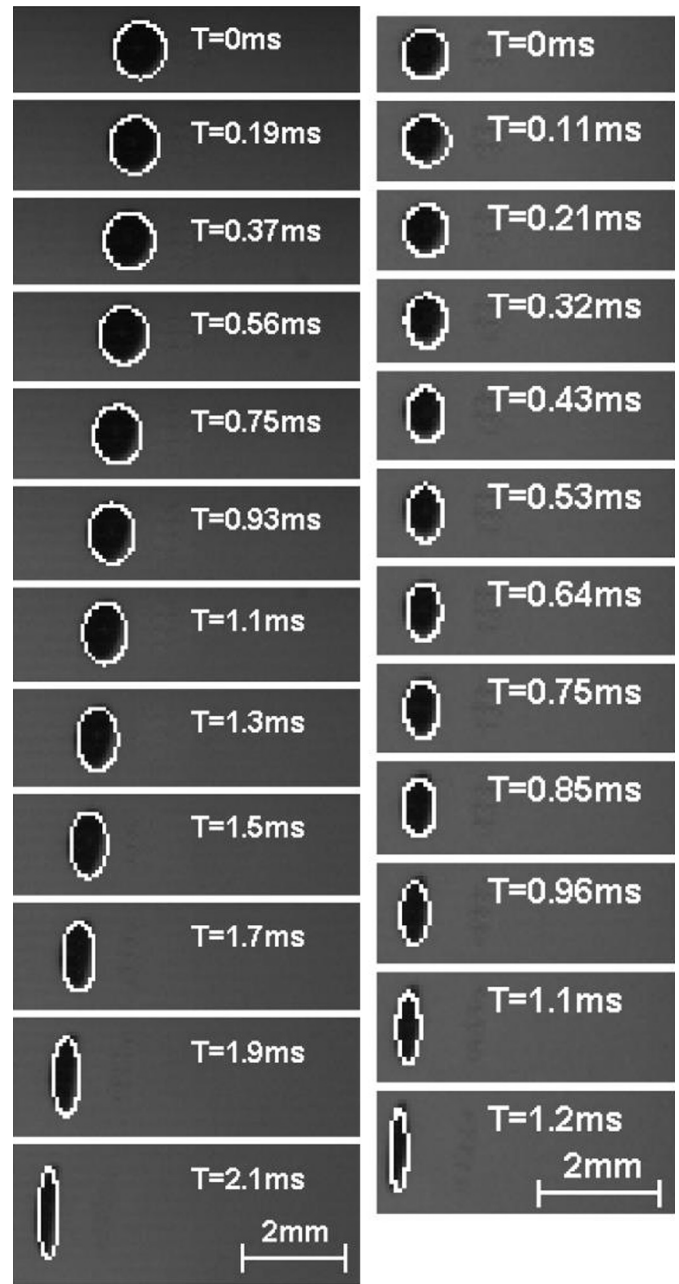

Fig. 13. Comparison between photographed and computed droplet shapes (superimposed white lines) as a function of time for cases: $R_c = 0.103$ m, $R_d = 513$ μm, and $U_m = 91$ m/s (left), and $R_c = 0.070$ m, $R_d = 388$ μm, and $U_m = 71$ m/s (right).

on top of the droplet images obtained from the experimental tracking system. The snapshots shown in Fig. 13 were taken at small time intervals to allow for a better comparison of the theoretical and experimental droplet shapes. This means that if the different snapshots of the droplet were presented in the same spatial reference frame, the droplet images would overlap creating confusion. Then, Fig. 14 shows both theoretical and experimental droplet shape and trajectory (for the two selected cases) using a larger time interval that allows for the pictures to be superimposed without overlapping. These two figures show a reasonable agreement between the predictions afforded by the theoretical model and the experimental data.

Now, it is pertinent to evaluate the issue of the relative importance of the quasi-steady, C_{D1}, and unsteady, C_{D2}, components of the drag coefficient in relations (5)–(7). To this end, both compo-
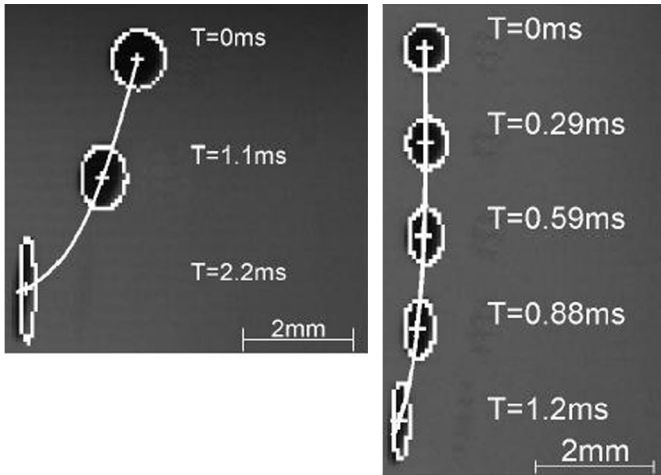
Fig. 14. Counterpart of Fig. 14 with the theoretical droplet trajectories (white lines) superimposed on the actual droplets images.
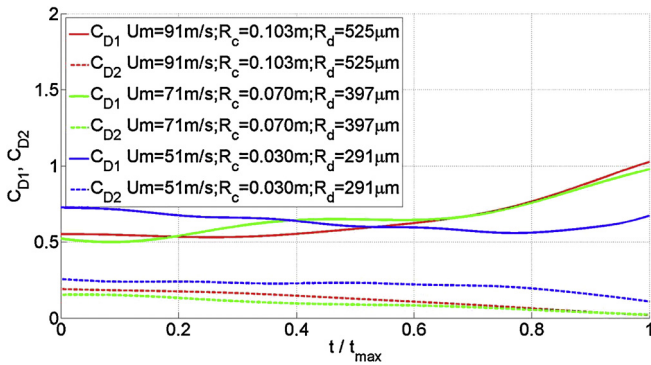

Fig. 15. Comparison between the quasi-steady, C_{D1}, and unsteady, C_{D2}, components of the drag coefficient in relations (5)–(7) for three representative cases.
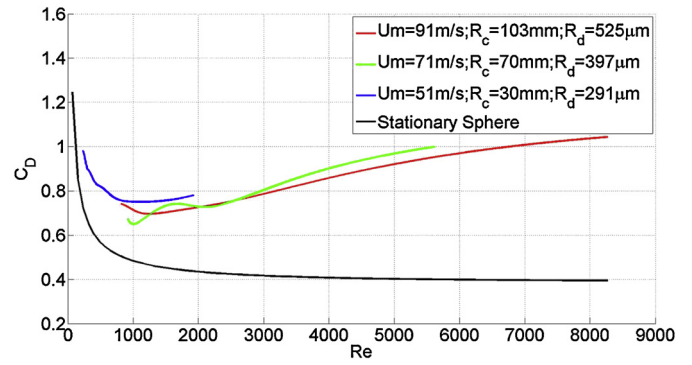

Fig. 16. Drag coefficient versus instantaneous Reynolds number for three different experimental cases. The drag coefficient of the stationary sphere is included for comparison purposes.
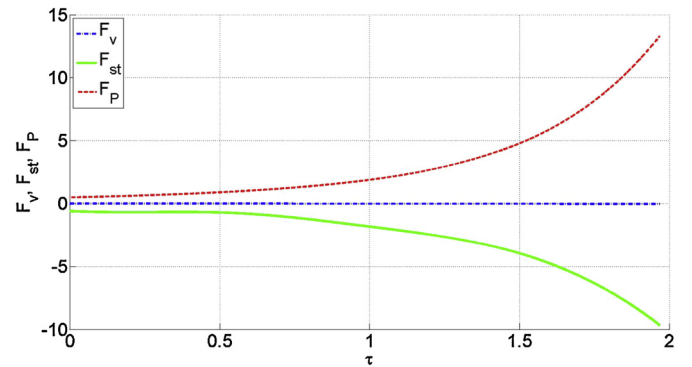

Fig. 17. Evaluation of terms in equation (3) for the case $R_c = 0.103$ m, $R_d = 513$ μm, and $U_m = 91$ m/s.

nents have been plotted in Fig. 15 for three representative cases. It could be observed that the quasi-steady component is always larger than the unsteady one but the latter cannot be neglected (if accurate results are sought) because it is, typically, of the order of 25% of the former. This means that, at least in the parametric space of parameters that have been considered in this experimental campaign, the unsteady component of the drag coefficient should not be neglected. It is also of interest to plot the total drag coefficient ($C_D = C_{D1} + C_{D2}$) as a function of the instantaneous Reynolds number that the droplet senses. This is done in Fig. 16 where the drag coefficient of an equivalent stationary sphere is also plotted for comparison purposes. As it could be observed, in the three cases that are presented in Fig. 16 (that are representative of the whole set of experimental cases that have been addressed in this study), the total drag coefficient is always larger than the steady sphere one. Also, the tendency is also different because the total C_D grows along with the Reynolds number while the steady sphere C_D decreases.

Finally, and for the sake of completion, the three terms in the right hand side of equation (3) are plotted separately to allow for comparison and, also, to check the hypothesis that has been made that the viscous force is much smaller than the surface tension force and the pressure force. To this end, once a representative case has been computed (the case parameters were $R_c = 0.103$ m, $R_d = 513$ μm, and $U_m = 91$ m/s) it solution was used to compute *a posteriori* the viscous force. The comparison between the three terms is shown in Fig. 17 where it could be observed that the

results obtained are consistent with the hypothesis that has been made in equation (3).

5. Conclusions

A theoretical model has been presented that predicts droplet trajectory and deformation in the vicinity of an incoming airfoil. The model is of interest both to gain a better understanding of droplet trajectories in some flows of aeronautics interest, and to provide an alternate formulation to researchers that develop numerical flow solvers in the field of icing conditions simulations. The model has been tested and calibrated using a series of dedicated experimental tests in a rotating arm facility. The novelty of the study consists on the fact that it accounts for the actual flow acceleration profile that the droplet senses as the airfoil closes on it. This is in contrast to other more basic-physics oriented studies in which shock tube type acceleration profiles are considered. The conclusions that have been obtained are, basically, two.

First, it is worth mentioning that a relatively simple model based on droplet dynamics and deformation (three ordinary differential equations) is enough to predict with reasonable accuracy droplet trajectory in the conditions that have been considered. The model can be said to have a "global" character because it implements force formulations that are "global" themselves. For example, the pressure force does not depend on the actual local coordinate on the droplet surface but it is modeled after a "global" coefficient. This suggests that the two problems of: a) the onset and further development of flow instabilities leading to droplet deformation and eventual break-up, and b) computation of droplet trajectory, are loosely coupled only. That is, once the conditions that define the basic type of deformation and break-up are set, the droplet trajectory can be modeled somewhat independently. For

example, in the parametric range of cases that have been considered, the assumption that the droplet deforms following the shape of a spheroid appears to be sufficient for trajectory prediction purposes.

The second question to be noted is that in the cases that have been addressed in the experimental campaign, implementation of an unsteady term in the aerodynamics drag model (the so-called acceleration parameter) is essential to allow for model accuracy. The issue of separating the drag into quasi-steady and unsteady parts (each one with its own modeling) is somewhat controversial and no claim is made in this article regarding its generalization. The only thing that can be said it that for the range of parameters under consideration in the present experimental campaign, the unsteady part of the drag coefficient was critically needed to compute trajectories that compared well to the observed trajectories. Regarding the unsteady drag model itself, the main differences between the model proposed in this article and previous results put forward by other researchers are two:

a) In the present model the acceleration parameter includes, also, the time dependent droplet dimension in the slip velocity-wise direction. This parameter was not considered in formulations described previously in the literature. In this sense, it could be said that its present inclusion makes sense because of the fact that droplets deformed significantly in these rotating arm experiments. It is to be noted that in other experimental studies researchers sometimes used droplets manufactured out of materials (plastic type) that did not allow for large deformations. On the Fluid Mechanics side, the reason for the implementation of the unsteady drag term is based on the fact that in an accelerating (or decelerating flow) the size of the recirculation region downstream of the droplet changes continuously; and the dynamics of this change affects the drag evolution. Then, in this regard, it is important to modify the acceleration parameter so as to account for information on droplet continuous deformation in the slip velocity-wise direction that, in turn, also affects the dynamics of the recirculation region.

b) The coefficient that multiplies the modified acceleration parameter in the present model is 9. In other studies dealing with different experimental setups, researchers found that this coefficient was dependent, also, on some other parameter(s) of the problem. However, in the present study it was found that for the range of parameters under consideration, the coefficient was always 9.

Finally, it should be said that the previous conclusions only apply for the cases that consider the flow acceleration profile generated by an incoming airfoil. This means that these conclusions cannot be extrapolated to other situations. A systematic study on the influence that functionally different acceleration profiles may have on droplet deformation and droplet trajectory is out of the scope of the present study.

Conflict of interest statement

We wish to confirm that there are no known conflicts of interest associated with this publication and there has been no significant financial support for this work that could have influenced its outcome.

Acknowledgements

References

[1] N. Kabaliuk, M.C. Jermy, E. Williams, T.L. Laber, M.C. Taylor, Experimental validation of a numerical model for predicting the trajectory of blood drops in typical crime scene conditions, including droplet deformation and breakup, with a study of the effect of indoor air currents and wind on typical spatter drop trajectories, Forensic Sci. Int. 245 (2014) 107–120.

[2] J. Petera, L.R. Weatherley, A.P. Hume, T. Gawrysiak, A finite element algorithm for particle/droplet trajectory tracking, tested in a liquid–liquid system in the presence of an external electric field, Comput. Chem. Eng. 31 (2007) 1369–1388.

[3] J. Petera, D. Rooney, L.R. Weatherley, Particle and droplet trajectories in a nonlinear electrical field, Chem. Eng. Sci. 53 (22) (1998) 3781–3792.

[4] M.M. Mohebil, J.R.G. Evans, The trajectory of ink-jet droplets: modeling and experiment, Chem. Eng. Sci. 60 (2005) 3469–3476.

[5] A. Sinha, R.S. Prakash, A.M. Mohan, R.V. Ravikrishna, Airblast spray in crossflow – structure, trajectory and droplet sizing, Int. J. Multiph. Flow 72 (2015) 97–111.

[6] O.O. Taskiran, M. Ergeneman, Trajectory based droplet collision model for spray modeling, Fuel 115 (2014) 896–900.

[7] Z. Yang, K. Krieger, T. Lunt, F. Brochard, J.-L. Briancon, R. Neu, R. Dux, A. Janzer, S. Potzel, T. Pütterich, 3D trajectories re-construction of droplets ejected in controlled tungsten melting studies in ASDEX Upgrade, J. Nucl. Mater. 438 (2013) 5846–5851.

[8] T.C.S. Rendall, C.B. Allen, Finite-volume droplet trajectories for icing simulation, Int. J. Multiph. Flow 58 (2014) 185–194.

[9] F. Saeed, C. Brette, M. Fregeau, O. Trifu, I. Paraschivoiu, A three-dimensional water droplet trajectory and impingement analysis program, in: 23rd AIAA Applied Aerodynamics Conference, 6–9 June 2005, Toronto, Ontario, Canada, 2005, AIAA 2005-4838.

[10] M. Papadakis, S.-C. Wong, A. Rachman, K.E. Hung, G.T. Vu, C.S. Bidwell, Large and small droplet impingement data on airfoils and two simulated ice shapes, NASA/TM-2007-213959, 2007.

[11] A.L. Reehorst, M. Ibrahim, Investigation of water droplet trajectories within the NASA icing research tunnel, NASA/TM 107023.

[12] S.K. Aggarwal, F. Peng, A review of droplet dynamics and vaporization modeling for engineering calculations, J. Eng. Gas Turbines Power 117 (1995) 453–461.

[13] R. Schmehl, Advanced modeling of droplet deformation and breakup for CFD analysis of mixture preparation, in: 18th Annual Conference on Liquid Atomization and Spray Systems, ILASS-Europe, 9–11 September 2002, Zürich, Schweiz, 2002.

[14] M.B. Bragg, A similarity analysis of the droplet trajectory equation, AIAA J. 20 (12) (1982) 1681–1686.

[15] M.R. Maxeya, J.J. Riley, Equation of motion for a small rigid sphere in a nonuniform flow, Phys. Fluids 26 (4) (1983) 883–889.

[16] T.R. Auton, J.C.R. Hunt, M. Prud´Homme, The force exerted on a body in inviscid unsteady non-uniform rotational flow, J. Fluid Mech. 197 (1988) 241–257.

[17] L.-P. Hsiang, G.M. Faeth, Drop deformation and breakup due to shock wave and steady disturbances, Int. J. Multiph. Flow 21 (4) (1995) 545–560.

[18] L. Zhang, C. Yang, Z.-S. Mao, Unsteady motion of a single bubble in highly viscous liquid and empirical correlation of drag coefficient, Chem. Eng. Sci. 63 (2008) 2099–2106.

[19] A.K. Flock, D.R. Guildenbecher, J. Chen, P.E. Sojka, H.-J. Bauer, Experimental statistics of droplet trajectory and air flow during aerodynamic fragmentation of liquid drops, Int. J. Multiph. Flow 47 (2012) 37–49.

[20] T.G. Theofanous, Aerobreakup of Newtonian and viscoelastic fluids, Annu. Rev. Fluid Mech. 43 (2011) 661–690.

[21] L.A. Zarrabeitia, F.Z. Qureshi, D.A. Aruliah, Stereo reconstruction of droplet flight trajectories, IEEE Trans. Pattern Anal. Mach. Intell. 37 (4) (2015) 847–861, http://dx.doi.org/10.1109/TPAMI.2014.2353638.

[22] T.G. Theofanous, G.J. Li, On the physics of aerobreakup, Phys. Fluids 20 (2008) 052103.

[23] S. Temkin, H.K. Mehta, Droplet drag in an accelerating and decelerating flow, J. Fluid Mech. 116 (1982) 297–313.

[24] O. Igra, K. Takayama, Shock tube study of the drag coefficient of a sphere in a non-stationary flow, Proc. R. Soc. A 442 (1993) 231–247.

[25] G. Jourdan, L. Houas, O. Igra, J.-L. Estivalezes, C. Devals, E.E. Meshkov, Drag coefficient of a sphere in a non-stationary flow: new results, Proc. R. Soc. A 463 (2007) 3323–3345.

[26] S. Sor, A. Garcia-Magariño, Modeling of droplet deformation near the leading edge of an airfoil, J. Aircr. 52 (2015) 1838–1846.

[27] E.A. Ibrahim, H.Q. Yang, A.J. Przekwas, Modeling of spray droplet deformations and breakup, J. Propuls. Power 9 (1993) 651–654.

[28] A. Garcia-Magariño, S. Sor, A. Velazquez, Experimental characterization of water droplet deformation and breakup in the vicinity of a moving airfoil, Aerosp. Sci. Technol. 45 (2015) 490–500.

[29] E. Iuliano, G. Mingione, F. Petrosino, F. Hervy, Eulerian modeling of large droplet physics toward realistic aircraft icing simulation, J. Aircr. 48 (2011) 1621–1632.

[30] M. Rudeno, Empirical choice of histograms and kernel density estimators, Scand. J. Stat. 9 (2) (1982) 65–78.